Hindawi
Advances in Civil Engineering
Volume 2020, Article ID 8850250, 16 pages
https://doi.org/10.1155/2020/8850250

Research Article

Uniaxial Experimental Study of the Deformation Behavior and Energy Evolution of Conjugate Jointed Rock Based on AE and DIC Methods

Jiliang Pan,[1] Xu Wu,[2] Qifeng Guo ,[1,3] Xun Xi,[4] and Meifeng Cai[1]

[1]*School of Civil and Resource Engineering, University of Science and Technology Beijing, Beijing 100083, China*
[2]*Beijing Municipal Engineering Research Institute, Beijing 100037, China*
[3]*State Key Laboratory of Coal Resources in Western China, Xi'an University of Science and Technology, Xi'an 710054, China*
[4]*Department of Civil and Environmental Engineering, University of Strathclyde, Glasgow G1 1XJ, UK*

Correspondence should be addressed to Qifeng Guo; guoqifeng@ustb.edu.cn

Received 11 June 2020; Revised 20 July 2020; Accepted 26 August 2020; Published 10 September 2020

Academic Editor: Fengqiang Gong

Conjugate joint is one of the most common joint forms in natural rock mass, which is produced by different tectonic movements. To better understand the preexisting flaws, it is necessary to investigate joint development and its effect on the deformation and strength of the rock. In this study, uniaxial compression tests of granite specimens with different conjugate joints distribution were performed using the GAW-2000 compression-testing machine system. The PCI-2 acoustic emission (AE) testing system was used to monitor the acoustic signal characteristics of the jointed specimens during the entire loading process. At the same time, a 3D digital image correlation (DIC) technique was used to study the evolution of stress field before the peak strength at different loading times. Based on the experimental results, the deformation and strength characteristics, AE parameters, damage evolution processes, and energy accumulation and dissipation properties of the conjugate jointed specimens were analyzed. It is considered that these changes were closely related to the angle between the primary and secondary joints. The results show that the AE counts can be used to characterize the damage and failure of the specimen during uniaxial compression. The local stress field evolution process obtained by the DIC can be used to analyze the crack initiation and propagation in the specimen. As the included angle increases from 0° to 90°, the elastic modulus first decreases and then increases, and the accumulative AE counts of the peak first increase and then decrease, while the peak strength does not change distinctly. The cumulative AE counts of the specimen with an included angle of 45° rise in a ladder-like manner, and the granite retains a certain degree of brittle failure characteristics under the axial loading. The total energy, elastic energy, and dissipation energy of the jointed specimens under uniaxial compression failure were significantly reduced. These findings can be regarded as a reference for future studies on the failure mechanism of granite with conjugate joints.

1. Introduction

Rock mass is discontinuous because of the movement and development of the crust. The joint, fissure, and fault fracture are the typical modes of this discontinuation. The most common joint geometries in natural rock mass are parallel joints and conjugate joints (also called *X*-shape intersecting joints), which are generated by different geotectonic movements [1, 2]. It is generally assumed that the failure of rock involves the growth and interaction of preexisting joints. The geometric configuration of joints has a paramount influence on the strength and deformation behavior of the jointed rock mass [3–5]. Many studies have considered the influence of joint geometries on the overall mechanical behavior of rock mass, the vast majority of which have involved testing on rock-like materials with artificially embedded joints [6–10]. For example, Brace and Bombolakis [11] carried out uniaxial and biaxial compression tests on brittle rock specimens with a single inclined crack. Griffith attributed the discrepancy between the observed fracture

strength of crystals and the theoretical cohesive strength to the presence of flaws in brittle materials. More severe stresses are raised by sharper natural defects, which are assumed to be present in all brittle materials, known as Griffith cracks. Hoek and Bieniawski [12] studied the initiation and propagation of a single Griffith crack in a biaxial compressive stress field. Bobet and Einstein [13] studied the behavior of fracture coalescence under uniaxial and biaxial compression, using gypsum specimens with two preexisting parallel joints. Chen et al. [14] investigated the combined influence of joint inclination angle and joint continuity factor on deformation behavior of jointed rock mass for gypsum specimens with a set of nonpersistent open flaws in uniaxial compression and revealed that the deformation behavior of the jointed rock mass was correlated to the closure of preexisting joints. Furthermore, many other experimental studies on the strength and deformation behavior of multiple joints with different geometries have been extensively conducted [15–18].

Acoustic emission (AE) testing technology is an effective means to study the propagation of defects in brittle materials, such as rocks. At present, this technology is widely used to study the internal damage and fracture behavior of rock materials [19–23]. The researchers use AE parameters to study fracture characteristics and processes of rocks, such as AE counts, amplitude, average frequency, duration, rise time, and energy. Eberhardt et al. [24] studied the failure process of the Lac Du Bonnet granite by the AE technology and found that the AE response is markedly different before and after new crack initiation. Rudajev et al. [25] disclosed the AE characteristics of the rock failure process using a uniaxial compression test. Zhao et al. [26] investigated the spatial AE distribution of granite samples with different surface precut cracks under uniaxial compression. Ganne et al. [27] studied brittle failure of rocks using the AE technology and divided the accumulated AE activity into four stages, which correspond to the generation, propagation, coalescence, and final failure of microcracks, respectively. Huang et al. [28] studied the effects of preexisting cracks on the mechanical properties of rocks and the coalescence process of cracks using AE technology and established the relationship between axial stress, AE counts, and the crack coalescence process. Zhang et al. [29] studied the AE characteristics of granite, marble, and salt rock in the process of damage and fracture and made a comparative analysis of their damage evolution trend.

Digital image correlation (DIC) is an optical and noncontact deformation measurement technique, which can be used to calculate the spatial distribution of the stress and the strain of the object during the deformation process. Recently, the DIC technique has been widely used in the field of experimental rock mechanics. Zhao et al. [30] studied the processes of crack initiation, propagation, and evolution and the distribution of stress field at the tip of crack and verified the results of DIC technique from the point of fracture mechanics. Munoz et al. [31] used DIC technique to analyze the strain field and eventual strain localization in the rock surface under uniaxial compression test. Furthermore, Cheng et al. [32] carried out uniaxial compression tests on a series of composite rock specimens with different dip angles, studied the evolution of axial strain field and the maximal strain field before and after the peak strength based on DIC technique, and analyzed the effect of bedding plane inclination on the deformation and strength during uniaxial loading. Yang et al. [33] carried out uniaxial compression tests on granite specimens containing a single crack and studied the effects of crack angle and heat treatment temperature on the mechanical properties and deformation failure behavior by using AE method and DIC technique.

According to the law of thermodynamics, the deformation of rock under loading is essentially a process of energy transformation, including energy absorption, evolution, and dissipation [34–37]. The theoretical and experimental studies have confirmed that energy plays a highly crucial role in the process of deformation and destruction of rock materials [38–42]. Cai [38] analyzed rockburst disasters in mining engineering from the prospect of energy accumulation theory. Gong et al. [39, 40] studied the energy storage and dissipation laws of rock materials in the uniaxial compression tests and three tension-type tests. Yang et al. [41] conducted conventional triaxial compression on marble and studied the resulting rock deformation damage and energy characteristics. Meng et al. [42] explored the energy accumulation, evolution, and dissipation characteristics in uniaxial cyclic loading and unloading compression of sandstone rock specimens under different loading rates.

Although considerable attention has been paid to the initiation and propagation of preexisting flaws in jointed rocks, the influence of conjugate joints on the overall mechanical properties of jointed rock mass and the underlying energy conversion mechanism remain less well understood. The AE of rock materials is a phenomenon where rock elastic strain energy is released in the deformation or failure process [43]. In this paper, uniaxial compression experiments of granite specimens with conjugate joints were performed using the GAW-2000 compression-testing machine system and the PCI-2 digital AE testing system. At the same time, the VIC-3D DIC System was used to study the evolution of local stress field before the peak strength at different loading times. Firstly, the whole process of the stress-strain curve was analyzed, and the deformation and strength characteristics of the jointed specimens during the loading process were discussed. Then, the AE counts and the damage evolution process were studied, and the differences in AE characteristics of the jointed specimens with different included angles were explored and the evolution of the stress concentration area on the specimen surface was analyzed. Finally, based on the energy conservation theory, the prefailure energy evolution of granite during uniaxial compression tests was examined. The results of this study will further the characterization of the deformation and failure process of conjugate jointed rock mass and will provide a reference for typical operations in rock engineering.

2. Experimental Methodology

2.1. Specimen Preparation. The joints that are not fully connected and persistent for the existence of rock bridges are termed as nonpersistent joints. It is an effective and

economical method to make jointed specimens by using rock-like materials such as concrete or gypsum for laboratory experiments [14–16]. In this method, the nonpersistent joints are usually produced by inserting different-sized metallic sheets into the rock-like specimen. The thickness of the metallic sheet determines the joint thickness, and the width of the metallic sheet determines the joint length. However, there are some shortcomings in this method. On the one hand, rock-like materials cannot reflect the real mechanical properties of rock materials. On the other hand, the preexisting joints produced by this method are relatively rough, and there are also some errors in the width and inclined angle.

In order to improve these deficiencies, this paper selects natural granite to make rock specimens. The granite used in the experiments is collected from Sanshandao gold mine, which is an underground gold mine located in Laizhou city, Shandong province, China. The granite is firstly processed into rock specimens with width of 50 mm, height of 100 mm, and thickness of 25 mm. The ends of each specimen were ground flat so that the error flatness of both end surfaces did not exceed 0.02 mm to avoid stress concentration during loading. To rigorously screen specimens, perform the following: (1) remove specimens with visible surface damage and visible flaws and (2) remove specimens whose size and flatness do not meet the standard requirement. To improve the precision of the preexisting joints, the specimen cutting and processing equipment were used, including a water jet cutter (WJC) and a wire cutting machine (WCM). Two joints with different lengths were cut at the center of the granite specimens by using the cutting equipment to study the effect of conjugate joints on the mechanical properties of granite specimens. As shown in Figure 1, the red line and the blue line represent the primary and the secondary joints, respectively. Both joints are discontinuous joints with a width of 0.3 mm, and the lengths of the primary and the secondary joints are 20 mm and 15 mm, respectively. It should be noted that the lengths of the primary and the secondary joints studied in this paper are only a special case. The angle between the primary joint and the loading direction is 90°, and the angle between the primary and the secondary joints is α, including 0°, 30°, 45°, 60°, and 90°.

2.2. Testing System and Procedure

2.2.1. Loading System Equipped with AE Monitoring. The uniaxial compression tests were carried out using a computer-controlled electrohydraulic servo compression-testing machine system (GAW-2000, Chaoyang Test Instrument Co., Ltd., Changchun, China). The GAW-2000 testing system can test the specimens in load or displacement control mode with simultaneous data recording. The maximum axial loading capacity of the servo-controlled system was 2000 kN, and the maximum displacement capacity was 100 mm. During the uniaxial compression tests, mechanical behavior and damage evolution of the preexisting jointed specimens were analyzed by the AE method. The AE instrument employed a PCI-2 AE monitoring system produced by American Physical Acoustics Corporation (PAC), which is composed of cable, amplifier (AMP), AE sensors, and data-acquisition control system. The sampling frequency range of the AE sensor is 1 kHz~3 MHz, and the A/D conversion resolution is 18 bits. The preamplifier is a 40 dB gain adjustable amplifier, which can amplify the signal 100 times. The AE system can perform real-time or postdata analysis and spectrum analysis. The uniaxial compression-testing system equipped with AE monitoring is presented in Figure 2.

2.2.2. DIC Measurement System. Using the DIC method, 3D displacements and strains are available at every point on the surface of specimen. The experimental equipment used in this study was the VIC-3D DIC System (Correlated Solutions, South Carolina, USA), which is a system for measuring and visualizing full-field, three-dimensional measurements of shape, displacement, and strain based on the principle of DIC. To achieve the effective correlation of the system, two main steps need to be completed before the experiment, namely, the charged couple discharge (CCD) cameras calibration and the speckle pattern of the specimens. Calibration of the system is essential in order to determine the best possible position of the two cameras, whereas the quality of the calibration also determines the accuracy of the DIC. This work can be done by calibration panel and VIC-3D software. For calculating the displacements with DIC, a reference image and an image after deformation must be recorded. Before the software VIC-3D calculates the displacements between these two images, an area of interest has to be set on the reference image. Therefore, the area of interest on the surface of specimen was coated with a white paint and sprayed with black aerosol to produce the required surface condition for the DIC. A setup of the rock specimens and the main equipment is illustrated in Figure 3.

2.2.3. Testing Procedure. During the test, the load and deformation values applied on the granite specimens were recorded simultaneously at a same data collection interval. The tests were conducted on the GAW-2000 compression-testing machine system by imposing a constant displacement speed of 0.03 mm/min until failure occurred. Two rigid steel blocks were placed between the loading frame and rock specimen. Vaseline was used as a coupler to load the specimen and AE sensors, and the AE sensors were attached on the two sides of the specimen by insulating tape to continuously record the AE activity during damage and fracture propagation within the specimen. The CCD cameras were used to take a series of images of the front surface of the specimen at a speed of one frame per second. These images were then analyzed by the VIC-3D software to determine the whole area displacement and stress distribution. The GAW-2000 loading machine, AE system, and the CCD camera were executed simultaneously to obtain the correlation of mechanical behavior, AE damage detection, and optical observation results.

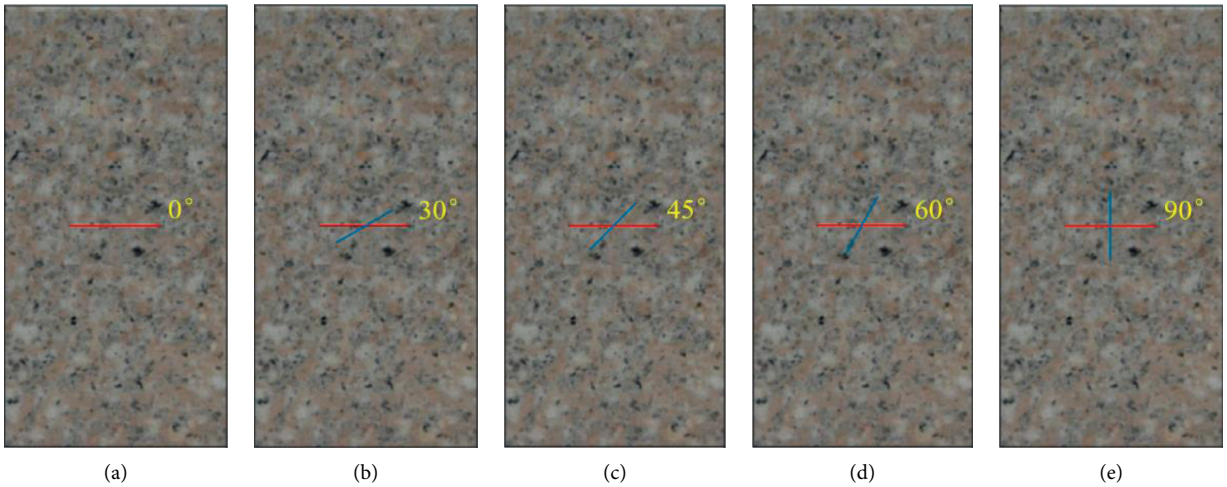

Figure 1: Preexisting conjugate joints with different included angles. (a) $\alpha = 0^{\circ}$, (b) $\alpha = 30^{\circ}$, (c) $\alpha = 45^{\circ}$, (d) $\alpha = 60^{\circ}$, and (e) $\alpha = 90^{\circ}$.

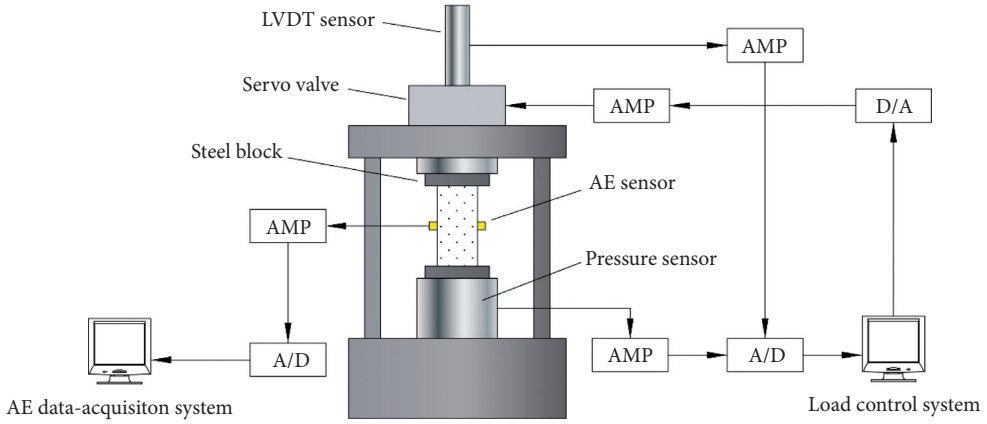

Figure 2: GAW-2000 testing system equipped with AE monitoring.

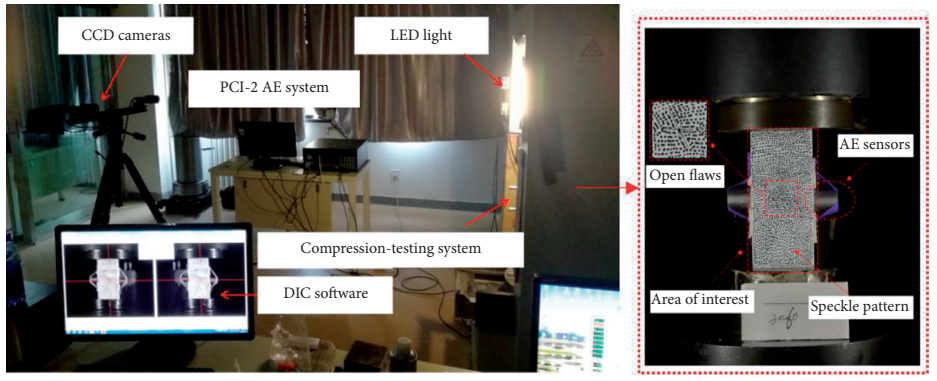

Figure 3: Rock specimens and main equipment.

3. Energy Calculation

Based on the laws of thermodynamics, the failure of rock material is the result of energy conversion. Assuming that a unit volume of material deforms by outer forces and that this physical process occurs in a closed system, the energy conversion can be defined according to the first law of thermodynamics

$$U = U_e + U_d, \tag{1}$$

where U_e and U_d are elastic strain energy density and dissipation energy density, respectively. U is the energy

density done by the outer force, which can be calculated as [36, 37]

$$U = \int_0^{\varepsilon_1} \sigma_1 d\varepsilon_1 + \int_0^{\varepsilon_2} \sigma_2 d\varepsilon_2 + \int_0^{\varepsilon_3} \sigma_3 d\varepsilon_3, \quad (2)$$

where σ_i and ε_i ($i = 1, 2, 3$) are the total stress and strain in the three principal stress directions, respectively. Under uniaxial compression conditions, equation (2) can be written as

$$U = \int_0^{\varepsilon_1} \sigma_1 d\varepsilon_1, \quad (3)$$

where σ_1 and ε_1 are the axial stress and axial strain of the rock element, respectively.

Figure 4 illustrates a typical stress-strain curve of rock, in which the lighter dotted area under the stress-strain curve represents the dissipated energy U_i^d, and the darker gridded area represents the releasable elastic energy U_i^e stored in rocks. The dissipation energy U_d results in internal damage and irreversible plastic deformation in the rock. The elastic energy U_e under uniaxial compression is given by the following [43]:

$$U_e = \frac{1}{2}\sigma_1 \varepsilon_1^e = \frac{1}{2E_j}\sigma_1^2, \quad (4)$$

where E_j is the elastic modulus of specimen with different angles and ε_1^e is the related elastic strain.

Substituting equations (3) and (4) into equation (1), the dissipation energy density can be expressed as

$$U_d = \int_0^{\varepsilon_1} \sigma_1 d\varepsilon_1 - \frac{1}{2E_j}\sigma_1^2. \quad (5)$$

4. Results and Discussion

4.1. Stress-Strain Curve. The uniaxial compression test is carried out by the AE method to evaluate the susceptibility of the granite specimens to deformation and failure. The stress-strain curves of the intact specimen and the conjugate jointed specimens under uniaxial compression are shown in Figure 5. In this section, the results of representative specimens are presented and analyzed. From the test results, the deformation and strength characteristics for the conjugate jointed specimen with different included angles were obtained. The overall stages of the stress-strain curves during the complete failure process could be divided into four stages, namely, initial compaction, elastic deformation, plastic deformation, and postpeak failure.

For the intact specimen, the elastic deformation stage is the longest among all specimens due to the uniform axial loading. In the stage of plastic deformation, the initiation, propagation, coalescence, and interaction of microcracks will induce the degradation of mechanical properties of specimens. The plastic deformation stage of the intact specimen is shorter than that of the jointed specimen. When the axial compressive stress reaches the peak strength, the specimen will be destroyed rapidly and enter the postpeak failure stage. The whole stress-strain curve shows a typical failure characteristic of elastic-brittle materials.

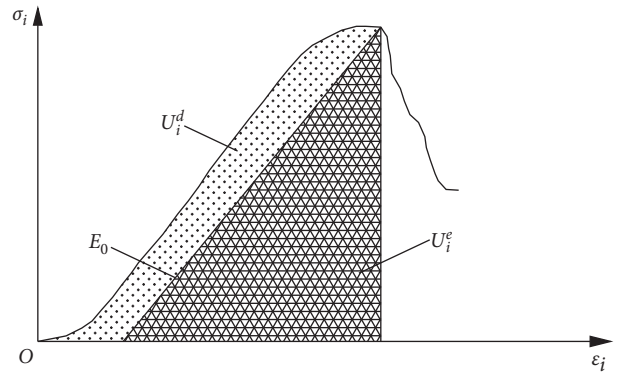

Figure 4: Relationship between dissipated energy and elastic energy.

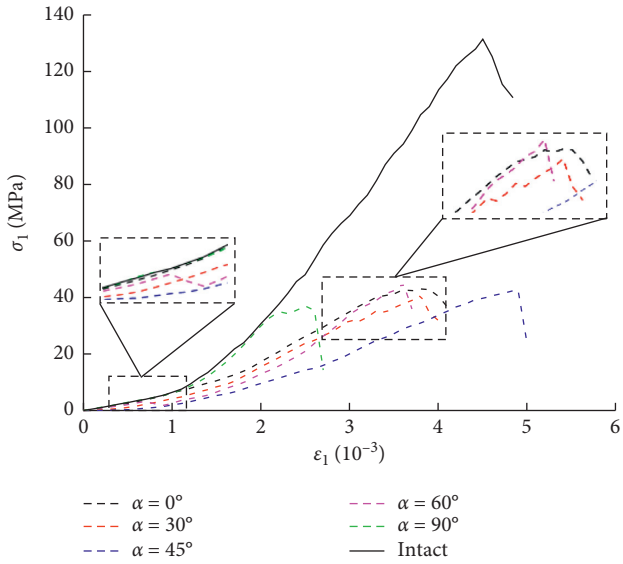

Figure 5: Stress-strain curves of the granite specimens.

For the conjugate jointed specimens, the overall trend of the initial compaction stage is similar to that of the intact specimen. In the initial compaction stage, the stress-strain curves of the specimen with $\alpha = 0^\circ$ and $\alpha = 90^\circ$ are the closest to those of the intact specimen, indicating that the preexisting joints have little effect on the compaction of this stage. It is worth noting that, at the initial compaction stage, the stress of the specimen with $\alpha = 60^\circ$ fluctuates obviously, which is due to the closure of the preexisting joints caused by the formation of new cracks. Under the same strain, the stress of the specimen with $\alpha = 45^\circ$ is lower than that of other jointed specimens, which indicates that the initial damage of the specimen with $\alpha = 45^\circ$ is the most serious among all the jointed specimens.

Due to the damage caused by the preexisting joints, the ability of the conjugate jointed specimen to resist external force deformation was reduced, and the elastic deformation stage was shorter than that of the intact specimen. The plastic deformation stage of the specimens with included angles of 0°, 30°, and 90° has significant fluctuation characteristics, which means that, under the axial loading, stress

concentration will occur around the preexisting joints and accelerate the microcracks initiation, propagation, and transfixion. With the release and redistribution of stress, the area of stress concentration gradually transfers to other parts of the specimen, which is the internal reason of the multistage drop of stress-strain curve. For the specimen with $\alpha = 30^{\circ}$, there are two small peaks before the peak, which illustrates that there are two incidents of local damage in the specimen which will not lead to the macroscopic failure of the specimen before the final failure. The peak strain of the conjugate jointed specimens is less than that of the intact specimen except for the specimen with $\alpha = 45^{\circ}$. With the increase of axial loading, new macrocracks will appear until the specimen loses its load-carrying capacity, which eventually leads to failure.

Table 1 shows the uniaxial compressive strength (UCS) and the elastic modulus of the intact and the jointed specimens. In order to characterize the damage evolution, two damage indices considering degradation of the UCS and the elastic modulus are introduced.

The normalized UCS was defined as the UCS of jointed specimen (σ_{cj}) divided by the UCS of intact specimen (σ_c), and the normalized elastic modulus was defined as the elastic modulus of jointed specimen (E_j) divided by the elastic modulus of intact specimen (E_0). The two damage indices were defined as follows:

$$D_c = 1 - \frac{\sigma_{cj}}{\sigma_c}, \qquad D_E = 1 - \frac{E_j}{E_0}. \tag{6}$$

The changes of two damage indices with the included angle are shown in Figure 6. It can be seen that the UCS and the elastic modulus of the conjugate jointed specimens are significantly reduced compared with the intact specimen, and the decrease range of the UCS was more obvious. The UCS of the jointed specimens is about 28%~35% of that of the intact specimen, which indicated that the preexisting joints have large initial damage to the specimen. The UCS of the jointed specimens is little affected by the included angle, and the change range is only about 7%. With the increase of the included angle, the elastic modulus decreases first and then increases. When $\alpha = 45^{\circ}$, the elastic modulus is the smallest, about 44% of that of the intact specimen, which means that the initial damage in this case is the largest. When the secondary joint is perpendicular to the primary joint (i.e., $\alpha = 90^{\circ}$), the initial damage is the smallest, and the elastic modulus is about 69% of that of the intact specimen.

4.2. Effect of Angle on the AE Counts and Damage Evolution. Each oscillation wave of electrical signal exceeding the threshold is an AE count, which is the external acoustic performance of the change of internal structure of rock, reflecting the intensity of AE activity and the evolution process of internal damage of rock. Figure 7 shows the AE counts and the accumulative AE counts during the loading of the jointed specimens with $\alpha = 0^{\circ}$. In the initial

Table 1: UCS and elastic modulus of specimens.

Parameter	Included angle α					Intact
	0°	30°	45°	60°	90°	
UCS (MPa)	43.14	40.94	42.45	46.33	36.94	131.43
Elastic modulus (GPa)	17.68	16.48	15.30	21.06	23.92	34.75

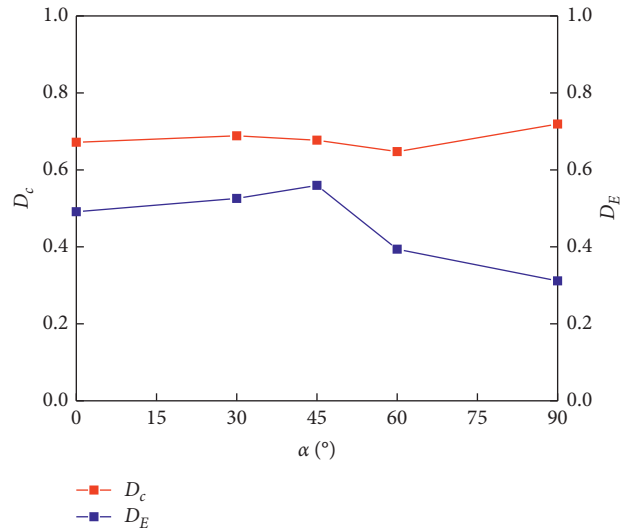

Figure 6: The changes of two damage indices with α.

compaction stage (I), the primary joints and the microcracks would be closed under the axial pressure. As a result, the AE counts were small and sporadic, with the accumulative counts increasing slowly. In the elastic deformation stage (II), the strain energy was continuously stored in the elastic matrix of the undamaged part of the granite, the specimen did not appear to undergo significant damage, the AE counts were small and tended to be smooth, and the accumulative AE counts growth was very slow. In the plastic deformation stage (III), the external loading gradually approaches the UCS of the specimen. Due to the influence of the preexisting joints, the stress-strain curve fluctuated significantly, and there are two peaks. The AE counts were raised significantly and the accumulative AE counts increased rapidly. In the postpeak failure stage (IV), the elastic energy accumulated in the rock is released quickly, and the specimen was seriously damaged. As the displacement continued to load, there was still a strong AE signal generated, and the accumulative AE counts also showed an upward trend. The reason for this is that the cracks previously generated further expanded and penetrated, resulting in a more intense structural movement and friction between the block fragments.

To reveal the evolution characteristics of the stress field during the loading process of jointed specimen with $\alpha = 0^{\circ}$, a series of different times of interest were selected on the stress-time curve shown in Figure 7. The stress field of the specimen surface at these different times is shown in Figure 8. At the end of the initial compaction stage (I), the stress concentration area appears in the center of the specimen, and the elastic strain energy begins to accumulate. Two new stress concentration areas began to appear below the two

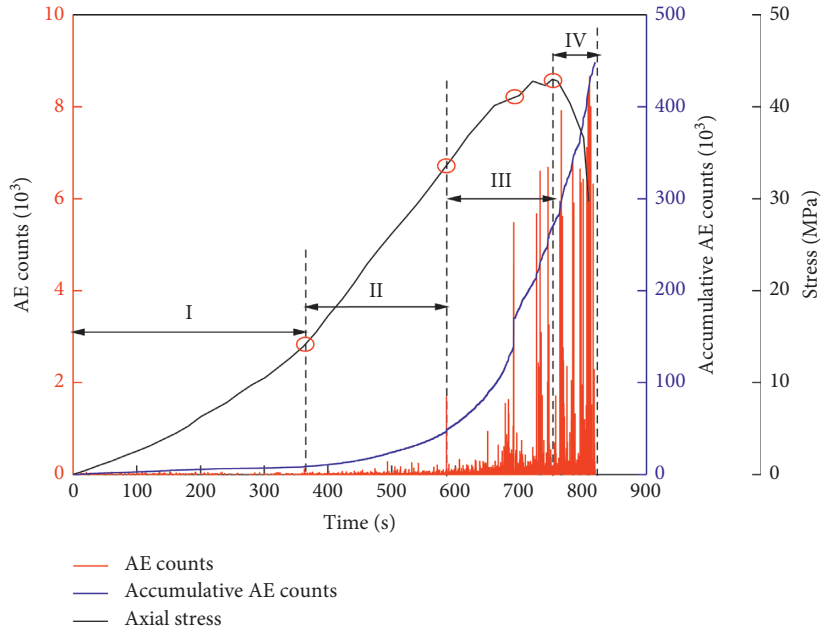

Figure 7: AE counts and accumulative AE counts of the jointed specimens with $\alpha = 0^\circ$.

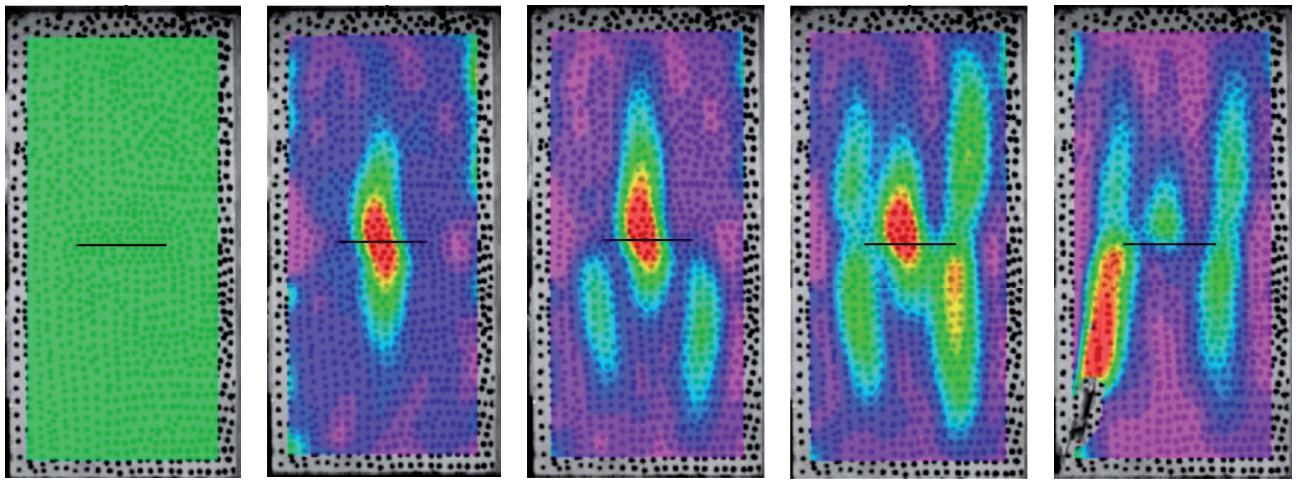

Figure 8: Stress field developed at different times for the specimen with $\alpha = 0^\circ$. (a) $t = 0$ s. (b) $t = 360$ s. (c) $t = 590$ s. (d) $t = 695$ s. (e) $t = 752$ s.

ends of the preexisting joint when the first AE event suddenly increased. Soon after that, the stress-time curve began to enter the plastic deformation stage (III). At the beginning of the plastic deformation stage (III), the H-shaped stress concentration area appeared, and the area gradually increased until the peak. At the peak point, the stress accumulation area is transferred to the lower-left corner of the specimen, and macrocracks begin to form.

Figure 9 shows the AE counts and the accumulative AE counts during the loading of the jointed specimens with $\alpha = 30^\circ$. There are more AE counts in the initial compression stage (I) and elastic deformation stage (II) than $\alpha = 0^\circ$. The plastic deformation stage (III) is longer, and the stress-time curve basically rises in the form of "ladder." At the plastic deformation stage (III), two distinct stress drops were observed on the curve, corresponding to two incidents of discrete damage. This indicates that there is not only the initiation of new cracks but also the further compaction, propagation, and coalescence of the preexisting joints in this stage. Every time the stress dropped, the AE counts experienced a large increase, and also a leap appeared in the accumulative AE counts correspondingly. The jointed specimens with $\alpha = 30^\circ$ also had a certain degree of ductility and residual strength in the postpeak failure stage (IV); many AE counts were recorded and the accumulative AE counts also increased. Figure 10 shows the stress field at different times on the stress-strain curve of the specimen with $\alpha = 30^\circ$. In the initial compression stage (I) and elastic

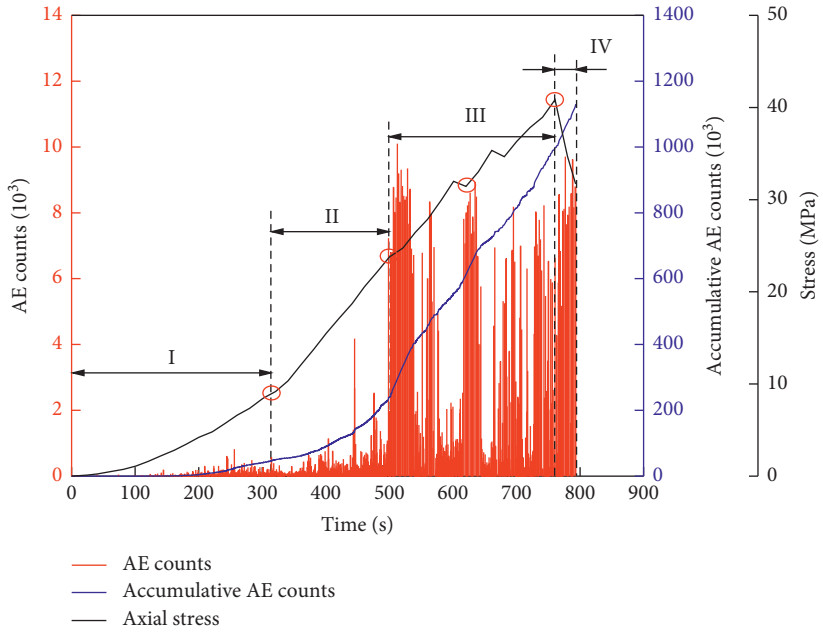

Figure 9: AE counts and accumulative AE counts of the jointed specimens with $\alpha = 30^\circ$.

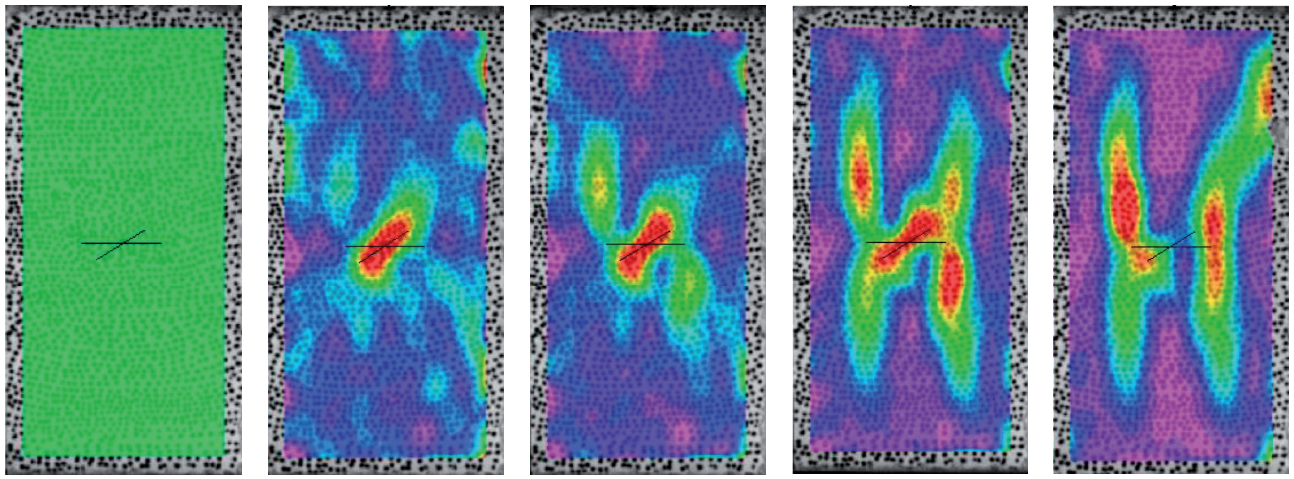

Figure 10: Stress field developed at different times for the jointed specimen with $\alpha = 30^\circ$. (a) $t = 0$ s. (b) $t = 315$ s. (c) $t = 500$ s. (d) $t = 620$ s. (e) $t = 760$ s.

deformation stage (II), the stress concentration will occur around the preexisting secondary joints. With the release and redistribution of stress, the area of stress concentration gradually transfers to other parts of the specimen, which is the internal reason of the multistage drop of the stress-time curve.

Figure 11 shows the AE counts and the accumulative AE counts of the jointed specimens with $\alpha = 45^\circ$ during the loading. Different from other joint specimens, the stress-time curve before the peak point does not have the characteristics of fluctuation, which means that the specimen with $\alpha = 45^\circ$ will not cause the preexisting joints initiation and propagation in advance. Furthermore, the accumulative AE counts curve does not show a stable growth; rather it shows a ladder-like rise. Because the plastic deformation stage (III) was not obvious, it can be considered that the stress-time curve before the peak point only has the initial compaction stage (I) and elastic deformation stage (II). In the elastic deformation stage (II), the AE counts at many time points suddenly increase, but the AE signals were not dense. Unlike the other jointed specimens, no significant increase in the AE counts of the jointed specimen with $\alpha = 45^\circ$ was detected for a period of time before reaching the peak point. These phenomena were proposed to be related to the multistage damage in the specimen, and the granite specimen with $\alpha = 45^\circ$ exhibited an obvious brittle failure characteristic. Figure 12 shows the stress field for the specimen with $\alpha = 45^\circ$ at the different loading times. Because

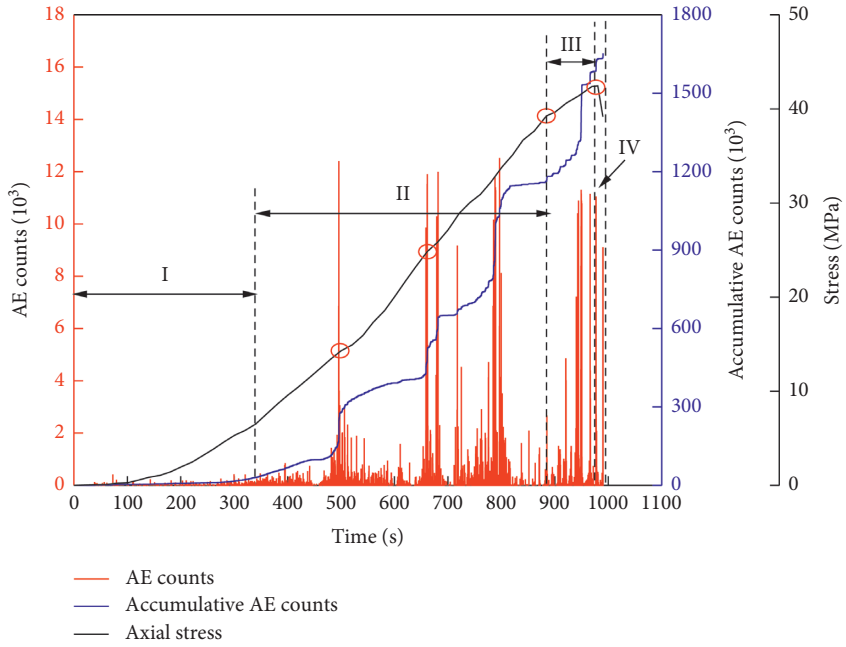

Figure 11: AE counts and accumulative AE counts of the jointed specimens with $\alpha = 45^{\circ}$.

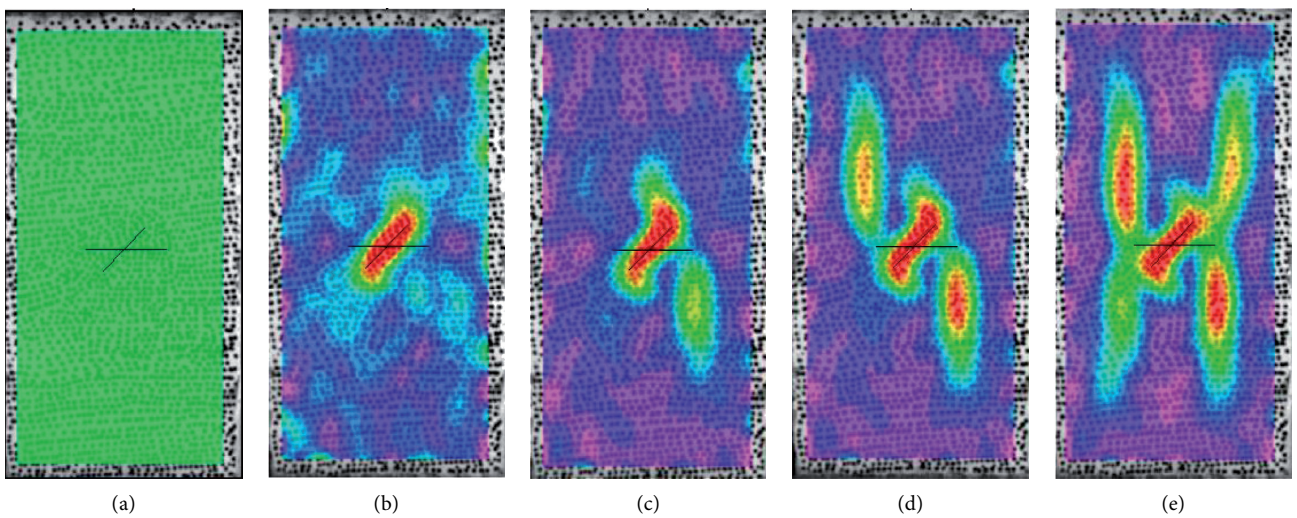

Figure 12: Stress field developed at different times for the jointed specimen with $\alpha = 45^{\circ}$. (a) $t = 0$ s. (b) $t = 500$ s. (c) $t = 660$ s. (d) $t = 890$ s. (e) $t = 975$ s.

the damage of the preexisting joints with $\alpha = 45^{\circ}$ to the mechanical properties of the specimen was smaller than those of other included angle joints, the specimen showed a certain degree of brittle deformation characteristics. During the loading process, the stress distribution was relatively uniform, and the area of stress concentration was small. This was also the reason why the stress-time curve did not undergo the obvious plastic deformation stage (III) but underwent brittle failure near the peak point. At the peak point, two localized highlights of the stress formed on the surface of the specimen were distributed on both sides of the secondary joint, and the whole stress field was H-shaped.

Figure 13 shows the AE counts and the accumulative AE counts during the loading of the jointed specimens with $\alpha = 60^{\circ}$. During the initial compaction stage (I), the stress-strain curve shows a steep fall, but the AE counts were still in the stationary phase, and the accumulative AE counts increased slowly, indicating that this is due to the compaction and closure of the preexisting joints, and there are no new crack initiation and propagation. Similar to the specimen with $\alpha = 45^{\circ}$, the plastic deformation stage (III) was not obvious, so it can be considered that the stress-time curve before the peak point only has the initial compaction stage (I) and elastic deformation stage (II). In the period from the

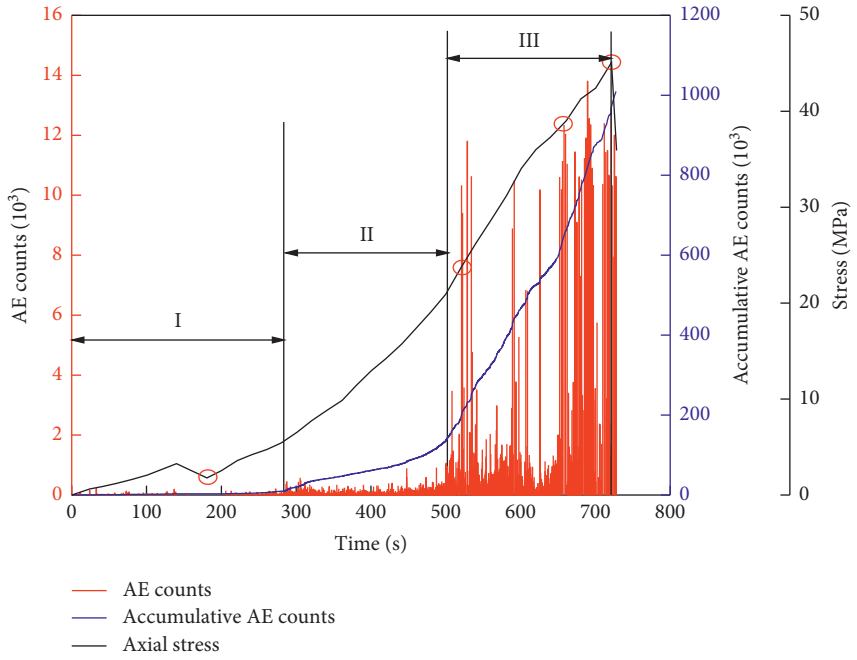

Figure 13: AE counts and accumulative AE counts of the jointed specimens with $\alpha = 60^\circ$.

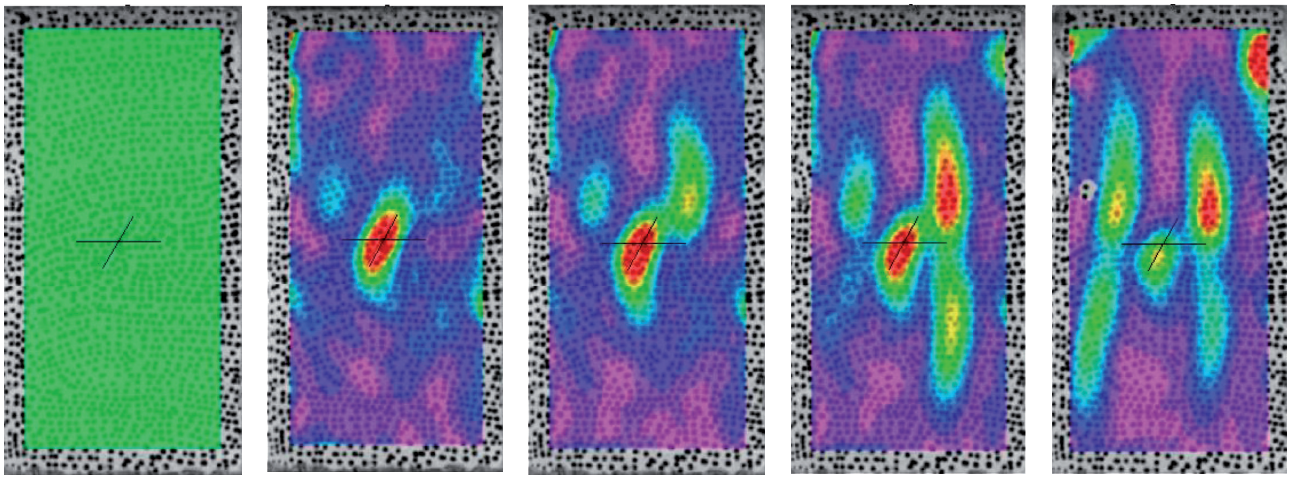

Figure 14: Stress field developed at different times for the jointed specimen with $\alpha = 60^\circ$. (a) $t = 0$ s. (b) $t = 180$ s. (c) $t = 525$ s. (d) $t = 655$ s. (e) $t = 720$ s.

beginning of the elastic deformation stage (II) to the peak point, there is no obvious fluctuation in the stress-time curve, and the AE counts were raised significantly and the accumulative AE counts increased rapidly. Figure 14 shows the stress field at different times on the stress-strain curve of the specimen with $\alpha = 60^\circ$. In the initial compaction stage (I), although there is a sudden stress drop point, the stress concentration area is not transferred or redistributed. In the stage of plastic deformation, a new stress concentration area appears at the upper end of the secondary joint, and two clear color gradients emerged in the stress field.

Figure 15 shows the AE counts and the accumulative AE counts during the loading of the jointed specimens with $\alpha = 90^\circ$. During the initial compaction stage (I) and elastic deformation stage (II), the AE counts were in the stationary phase, and the accumulative AE counts slowly increased. Same as the specimen with $\alpha = 60^\circ$, the plastic deformation stage (III) of the specimen with $\alpha = 90^\circ$ is very short. In the plastic deformation stage (III), there appears a sudden drop of stress in the stress-time curve, forming two peak points. The AE counts detected in a short period of time before the peak point was reached increased significantly, and the accumulative AE counts increased accordingly as the displacement continued to load. These results show that the AE characteristic can be used to characterize the damage and failure of the specimen during the loading process. Figure 16

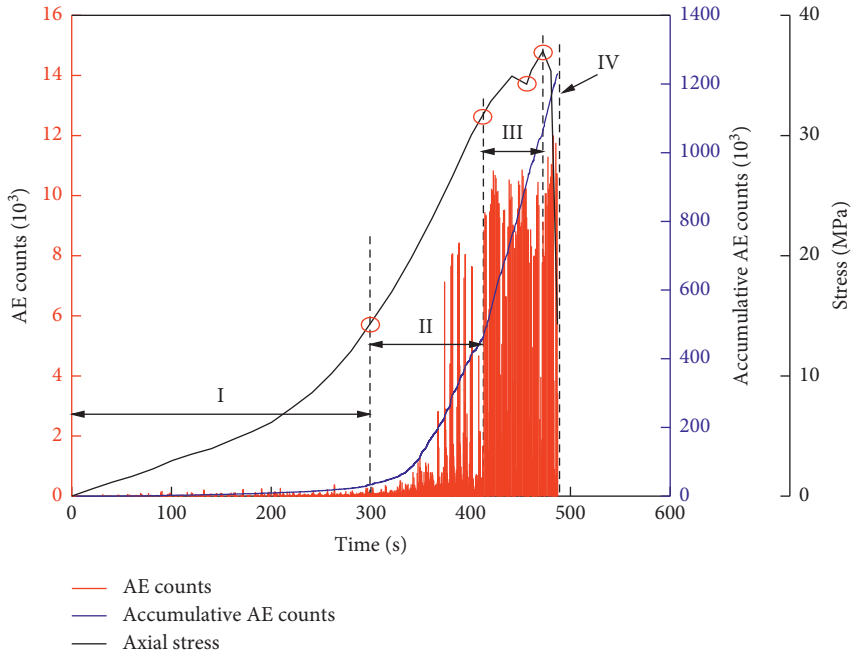

Figure 15: AE counts and accumulative AE counts of the jointed specimens with $\alpha = 90^\circ$.

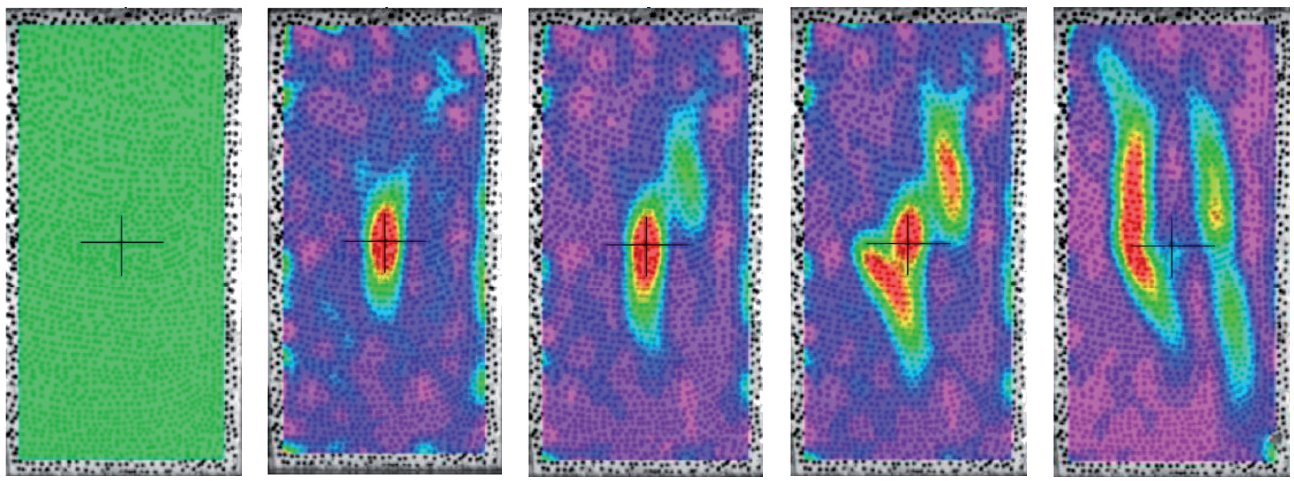

Figure 16: Stress field developed at different times for the jointed specimen with $\alpha = 90^\circ$. (a) $t = 0$ s. (b) $t = 300$ s. (c) $t = 410$ s. (d) $t = 455$ s. (e) $t = 470$ s.

shows the stress field for the specimen with $\alpha = 90^\circ$ at the different loading times. Before the plastic deformation stage (III), the stress concentration area is mainly distributed in the center of the specimen. With the increase of the axial loading, there appears a sudden drop point in the stress before the peak point is reached, some of the elastic strain energy was released, and the stress field was redistributed. At the peak point, the stress is concentrated on the diagonal of the specimen, which eventually causes the specimen to fail along the diagonal.

4.3. Effect of Angle on Energy Evolution. The energy evolution processes of rock specimens under the uniaxial compression test are shown in Figure 17. The initiation, propagation, coalescence, and interaction of microcracks in the process of loading lead to the deterioration and loss of the rock strength, which is the main cause of the energy dissipation. In other words, the energy dissipation is closely related to the attenuation of the strength, and the amount of the dissipation energy can be used to reflect the degree of damage of specimen in the process of axial loading. Because the granite

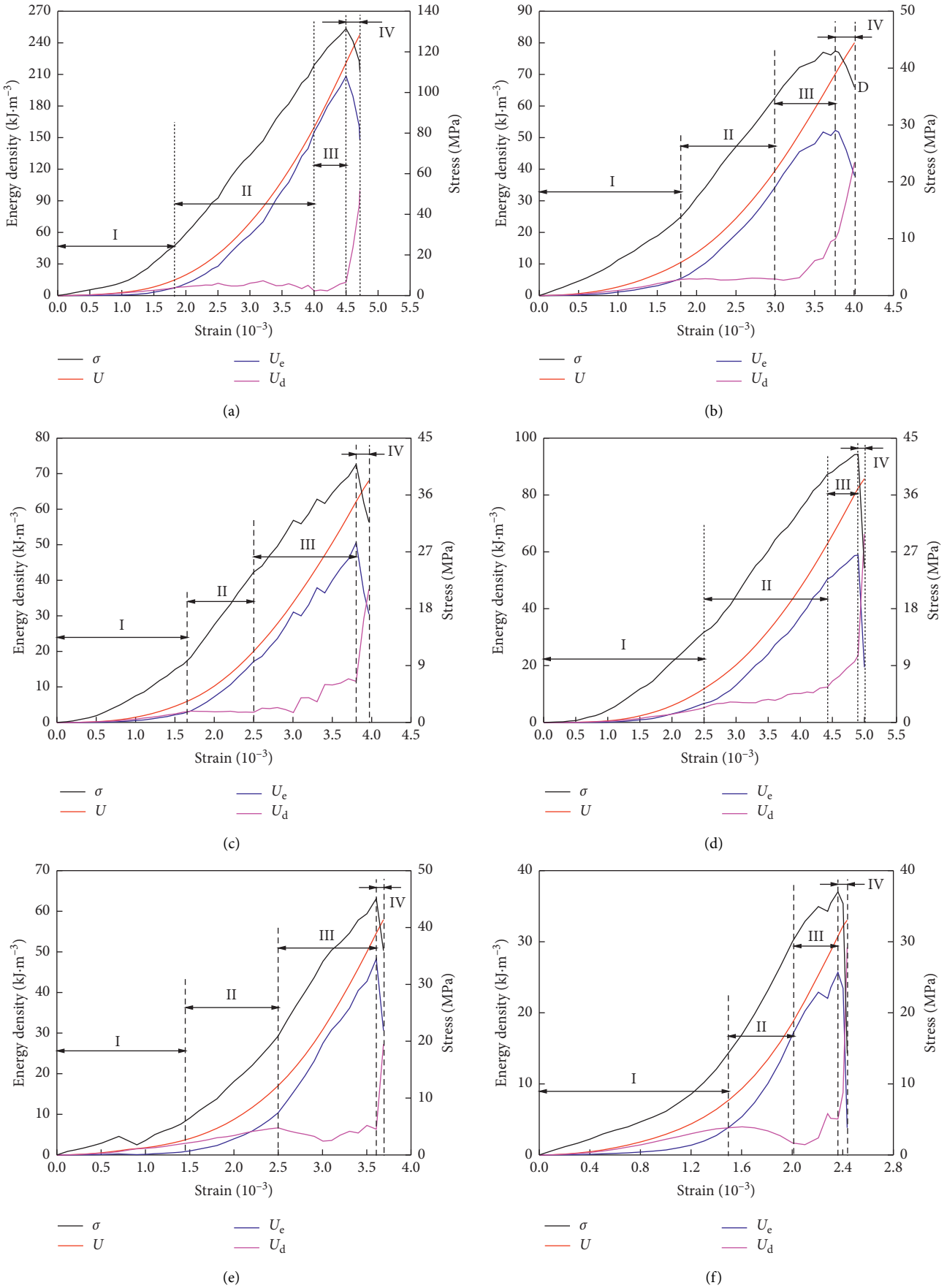

Figure 17: Energy evolution of rock specimen under UCS test. (a) Intact, (b) $\alpha = 0^{\circ}$, (c) $\alpha = 30^{\circ}$, (d) $\alpha = 45^{\circ}$, (e) $\alpha = 60^{\circ}$, and (f) $\alpha = 90^{\circ}$.

specimens contain many native holes and defects, the holes and defects would be closed under the initial pressure. At the initial compression stage, the total input energy increases nonlinearly with the strain, and most of the energy is consumed by the closure and friction of microcracks. At this time, the dissipation energy is generally greater than the elastic deformation energy. The closure of microcracks increases the effective contact area, increases the accumulation rate of elastic energy, and decreases the growth rate of dissipative energy until the curve of elastic energy intersects the curve of dissipative energy. Then, the growth rate of elastic energy is gradually greater than that of dissipation energy, which is consistent with the growth rate of total energy input into the system. After that, the deformation of the specimen began to enter the stage of elastic deformation.

At the elastic deformation stage, the total energy and the elastic energy increase linearly with the strain approximately, and the dissipation energy almost remains unchanged or even decreases. At this stage, the dissipative energy of the intact specimen is about $10\,kJ/m^3$. The dissipative energy of the conjugate jointed specimens is generally lower than that of the intact specimen, and the energy evolution is closely related to the included angle. The dissipated energy of the jointed specimens with included angles of 0°, 30°, and 45° in the elastic deformation stage is about $5\,kJ/m^3$, $3\,kJ/m^3$, and $7\,kJ/m^3$, respectively. At this time, the total input energy is almost completely converted into the elastic energy, and the dissipated energy is very little. The peak strain of the specimens with $\alpha = 60^\circ$ and $\alpha = 90^\circ$ is smaller than those of the other jointed specimens, and the elastic deformation stage is relatively short, while the decrease of the dissipation energy is obvious. This phenomenon shows that the microcracks or the preexisting joints in the rock specimens are further compressed and the proportion of the elastic energy is further increased.

At the plastic deformation stage, the external loading gradually approaches the UCS of rock specimen. With the rapid initiation and propagation of new cracks in the specimen, the dissipation energy begins to increase. Due to the strong brittleness of the intact specimen, when a large number of new cracks appear, the specimen will quickly reach the peak strength and then be fractured. Therefore, there is almost no plastic deformation stage in the complete specimen. At this stage, there is not only the initiation of new cracks but also the further expansion and transfixion of the preexisting joints, leading to the obvious increase of dissipation energy. For the jointed specimens with the angles of 0°, 30°, 60°, and 90°, the continuous accumulation of deformation leads to the stress concentration at the crack tip, thus accelerating the crack initiation and propagation. In this process, the accumulated elastic energy in rock specimen is released suddenly, and the curves of the elastic energy and the dissipation energy increase in the form of "ladder." At this stage, the dissipation energy of the jointed specimen with $\alpha = 45^\circ$ increases gradually, but it does not have the characteristic of ladder-like growth.

At the postpeak failure stage, the macrofracture occurs, the elastic energy accumulated in the rock is released quickly, and the internal cracks of the specimen are coalesced and penetrated rapidly. Then, the rock loses carrying capacity and shows obvious brittle characteristics. During this stage, the dissipation energy increases with the increase of strain, while the elastic energy decreases with the increase of strain, and the curves of the dissipation energy and the elastic energy intersect.

4.4. Peak Indexes. The peak energy indexes of the intact and the jointed specimens are shown in Table 2, and the comparison of peak energy and the accumulative AE counts of the jointed specimens is shown in Figure 18. It can be seen that the ability of accumulating elastic strain energy of the intact specimen is the strongest. The total elastic energy accumulated at the peak can reach $208.37\,kJ/m^3$, and the energy accumulation rate can reach 94.26%, indicating that most of the work done by the external force is converted into the elastic energy and stored in the intact rock matrix. When the axial stress reaches the UCS, the damage caused by the instantaneous release of the elastic energy is also the most serious. However, for jointed rock mass, the behaviors of the preexisting flaws propagation will consume energy, and the accumulation of the dissipation energy will lead to the jointed rock from original stable state to unstable state and finally to failure.

For the conjugate jointed specimens, because of the initial damage caused by the preexisting joints, the energy storage capacity of the specimen is weaker than that of the intact specimen, indicating that the ability to accumulate elastic energy is closely related to the included angle. Among them, the ability to accumulate elastic energy of the specimen with $\alpha = 45^\circ$ is the strongest, and the total accumulated elastic energy at the peak is $58.87\,kJ/m^3$, accounting for 71.4% of the total energy. It shows that the specimen with $\alpha = 45^\circ$ has strong brittleness deformation characteristics, and a large part of the work done by the external force was stored in the rock mass in the form of elastic energy, which was released instantly when the final failure occurs. The energy accumulation rate of the specimen with $\alpha = 60^\circ$ is 88.39%, which is the highest among all jointed specimens. The capability of accumulating elastic energy of the specimen with $\alpha = 90^\circ$ is the weakest, which is only $25.69\,kJ/m^3$ at the peak. Therefore, the specimen with $\alpha = 90^\circ$ will be destroyed first in all specimens.

As the included angle of conjugate joint increases from 0° to 90°, the accumulative AE counts of the peak increase first and then decrease. The number of peak cumulative AE counts of the specimen with $\alpha = 45^\circ$ is the biggest, which means that the joint specimens with this angle have strongest brittleness deformation ability. The peak accumulative AE counts of the specimen with $\alpha = 30^\circ$ are very close to those of the specimen with $\alpha = 60^\circ$. The peak cumulative AE counts of the specimen with $\alpha = 0^\circ$ are much smaller than those of other joint specimens, because the primary and secondary joints coincide, and the mechanical properties of the specimen are only affected by the primary joint. Compared with other conjugated joints, the single joint formed by overlapping of the primary and secondary joints has less

Table 2: Peak energy indexes of the intact and the jointed specimens.

α	Total energy (kJ/m^3)	Elastic energy (kJ/m^3)	Dissipation energy (kJ/m^3)	Energy accumulation rate (%)	Energy dissipation rate (%)
Intact	221.05	208.37	12.68	94.26	5.74
0°	70.17	52.29	17.88	74.52	25.48
30°	62.16	50.60	11.56	81.40	18.60
45°	82.45	58.87	23.58	71.40	28.60
60°	54.62	48.28	6.34	88.39	11.61
90°	30.75	25.69	5.06	83.54	16.46

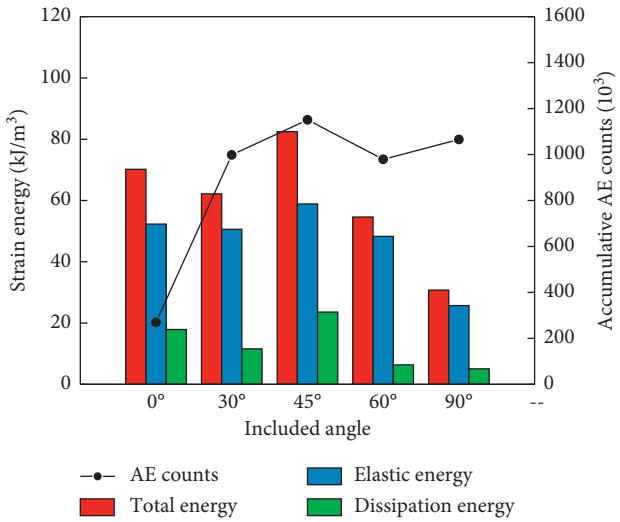

Figure 18: Comparison of peak energy and accumulative AE counts.

damage to the rock mass, so it retains the strength characteristics of the granite materials to a large extent.

5. Conclusions

Based on the uniaxial compression test and the AE test of the granite specimens with conjugate joints, the following points are summarized:

(1) The angle between the primary and the secondary joints has a significant effect on the stress-strain curve of the rock specimens. The stress-strain curve of the jointed specimens will enter the plastic deformation stage in advance, and the elastic deformation stage will be shorter, while the plastic deformation stage will be longer. The plastic deformation stage of the jointed specimens with included angles of 0°, 30°, and 90° has obvious stress fluctuation characteristics.

(2) The damage and deformation of jointed rock under different included angles can be described by accumulative AE counts. The accumulative AE counts of the specimen with $\alpha = 45°$ rise in a ladder-like manner, leading to multistage damage in the rock mass until the macrocracks occurred. The conjugate joints of 45° retain the brittleness of granite to some extent and show obvious brittleness failure characteristics under the axial loading. The accumulative AE counts of the specimen with $\alpha = 0°$ are the smallest and the rock mass still has strong brittleness. The AE duration time of the specimen with $\alpha = 90°$ is the shortest, but the growth rate of the accumulative AE counts curve is the largest.

(3) Compared with the intact specimen, the peak strength and the elastic modulus of the jointed specimens are significantly decreased, and the decrease range of the peak strength is more obvious. As the included angle increases from 0° to 90°, the elastic modulus first decreases and then increases, and the accumulative AE counts of the peak increase first and then decrease, while the peak strength does not change distinctly. The peak strain of the other specimens is less than that of the intact specimen except for the specimen with $\alpha = 45°$.

(4) The total energy, elastic energy, and dissipation energy of the uniaxial compression failure of the jointed specimens are significantly reduced compared with the intact specimen, and the ability of the specimens to accumulate the elastic energy is closely related to the included angle. Compared with other conjugated joints, the single joint formed by overlapping of the primary and secondary joints has less damage to rock mass and retains the strength characteristics of the granite materials to a large extent.

Data Availability

The experimental data used to support the findings of this study are included within the article.

Conflicts of Interest

The authors declare that there are no conflicts of interest regarding the publication of this paper.

Acknowledgments

The first author gratefully acknowledges financial support from China Scholarship Council. This research was funded by the Fundamental Research Funds for the Central Universities (no. FRF-TP-18-015A3) and the Key Laboratory of Western Mine Exploitation and Hazard Prevention of Ministry of Education (no. SKLCRKF1901).

References

[1] X. Liu, Q. Liu, Y. Kang, and Y. Pan, "Improved nonlinear strength criterion for jointed rock masses subject to complex stress states," *International Journal of Geomechanics*, vol. 18, no. 3, Article ID 04017164, 2018.

[2] B. Zhang, S. Li, X. Yang et al., "The coalescence and strength of rock-like materials containing two aligned *X*-type flaws under uniaxial compression," *Geomechanics and Engineering*, vol. 17, no. 1, pp. 47–56, 2019.

[3] G. Reik and M. Zacas, "Strength and deformation characteristics of jointed media in true triaxial compression," *International Journal of Rock Mechanics and Mining Sciences & Geomechanics Abstracts*, vol. 15, no. 6, pp. 295–303, 1978.

[4] Z. Y. Yang, J. M. Chen, and T. H. Huang, "Effect of joint sets on the strength and deformation of rock mass models," *International Journal of Rock Mechanics and Mining Sciences*, vol. 35, no. 1, pp. 75–84, 1998.

[5] M. Singh, K. S. Rao, and T. Ramamurthy, "Strength and deformational behaviour of a jointed rock mass," *Rock Mechanics and Rock Engineering*, vol. 35, no. 1, pp. 45–64, 2002.

[6] P. P. Wasantha, P. G. Ranjith, D. R. Viete, and L. Luo, "Influence of the geometry of partially-spanning joints on the uniaxial compressive strength of rock," *International Journal of Rock Mechanics and Mining Sciences*, vol. 50, pp. 140–146, 1997.

[7] X.-X. Yang, H.-W. Jing, C.-A. Tang, and S.-Q. Yang, "Effect of parallel joint interaction on mechanical behavior of jointed rock mass models," *International Journal of Rock Mechanics and Mining Sciences*, vol. 92, pp. 40–53, 2017.

[8] Q. Guo, J. Pan, M. Cai, and Y. Zhang, "Investigating the effect of rock bridge on the stability of locked section slopes by the direct shear test and acoustic emission technique," *Sensors*, vol. 20, no. 3, p. 638, 2020.

[9] Y. Liu, F. Dai, P. Fan, N. Xu, and L. Dong, "Experimental investigation of the influence of joint geometric configurations on the mechanical properties of intermittent jointed rock models under cyclic uniaxial compression," *Rock Mechanics and Rock Engineering*, vol. 50, no. 6, pp. 1453–1471, 2017.

[10] Y. Liu and F. Dai, "A damage constitutive model for intermittent jointed rocks under cyclic uniaxial compression," *International Journal of Rock Mechanics and Mining Sciences*, vol. 103, pp. 289–301, 2018.

[11] W. F. Brace and E. G. Bombolakis, "A note on brittle crack growth in compression," *Journal of Geophysical Research*, vol. 68, no. 12, pp. 3709–3713, 1963.

[12] E. Hoek and Z. T. Bieniawski, "Brittle fracture propagation in rock under compression," *International Journal of Fracture Mechanics*, vol. 1, no. 3, pp. 137–155, 1965.

[13] A. Bobet and H. H. Einstein, "Fracture coalescence in rock-type materials under uniaxial and biaxial compression," *International Journal of Rock Mechanics and Mining Sciences*, vol. 35, no. 7, pp. 863–888, 1998.

[14] X. Chen, Z. Liao, and X. Peng, "Deformability characteristics of jointed rock masses under uniaxial compression," *International Journal of Mining Science and Technology*, vol. 22, no. 2, pp. 213–221, 2012.

[15] R.-h. Cao, P. Cao, H. Lin, C.-z. Pu, and K. Ou, "Mechanical behavior of brittle rock-like specimens with pre-existing fissures under uniaxial loading: experimental studies and particle mechanics approach," *Rock Mechanics and Rock Engineering*, vol. 49, no. 3, pp. 763–783, 2016.

[16] S. Q. Yang, D. S. Yang, H. W. Jing, Y. H. Li, and S. Y. Wang, "An experimental study of the fracture coalescence behaviour of brittle sandstone specimens containing three fissures," *Rock Mechanics and Rock Engineering*, vol. 45, no. 4, pp. 563–582, 2012.

[17] S.-Q. Yang, X.-R. Liu, and H.-W. Jing, "Experimental investigation on fracture coalescence behavior of red sandstone containing two unparallel fissures under uniaxial compression," *International Journal of Rock Mechanics and Mining Sciences*, vol. 63, no. 63, pp. 82–92, 2013.

[18] X. Xi, S. Yang, and C.-Q. Li, "A non-uniform corrosion model and meso-scale fracture modelling of concrete," *Cement and Concrete Research*, vol. 108, pp. 87–102, 2018.

[19] X. Xi, X. Wu, Q. Guo, and M. Cai, "Experimental investigation and numerical simulation on the crack initiation and propagation of rock with pre-existing cracks," *IEEE Access*, vol. 8, Article ID 129636, 2020.

[20] Q. Guo, X. Wu, M. Cai, F. Ren, and J. Pan, "Crack initiation mechanism of pre-existing cracked granite," *Journal of the China Coal Society*, vol. 44, no. S2, pp. 476–483, 2019.

[21] X. Wu, "Crack initiation and failure mechanism of granite with single crack," *Geotechnical and Geological Engineering*, vol. 38, no. 1, pp. 651–661, 2020.

[22] X. Lai, J. Ren, F. Cui et al., "Study on vertical cross loading fracture of coal mass through hole based on AE-TF characteristics," *Applied Acoustics*, vol. 166, Article ID 107353, 2020.

[23] G. Shi, X. Yang, H. Yu, and C. Zhu, "Acoustic emission characteristics of creep fracture evolution in double-fracture fine sandstone under uniaxial compression," *Engineering Fracture Mechanics*, vol. 210, pp. 13–28, 2019.

[24] E. Eberhardt, D. Stead, B. Stimpson, and R. S. Read, "Identifying crack initiation and propagation thresholds in brittle rock," *Canadian Geotechnical Journal*, vol. 35, no. 2, pp. 222–233, 1998.

[25] V. Rudajev, J. Vilhelm, and T. Lokaǰíček, "Laboratory studies of acoustic emission prior to uniaxial compressive rock failure," *International Journal of Rock Mechanics and Mining Sciences*, vol. 37, no. 4, pp. 699–704, 2000.

[26] X. Zhao, Y. Li, R. Yuan, T. Yang, J. Zhang, and J. Liu, "Study on crack dynamic propagation process of rock samples based on acoustic emission location," *Chinese Journal of Rock Mechanics and Engineering*, vol. 26, no. 5, pp. 944–950, 2007.

[27] P. Ganne, A. Vervoort, and M. Wevers, "Quantification of pre-peak brittle damage: correlation between acoustic emission and observed micro-fracturing," *International Journal of Rock Mechanics and Mining Sciences*, vol. 44, no. 5, pp. 720–729, 2007.

[28] Y.-H. Huang, S.-Q. Yang, W.-L. Tian, W. Zeng, and L.-Y. Yu, "An experimental study on fracture mechanical behavior of rock-like materials containing two unparallel fissures under uniaxial compression," *Acta Mechanica Sinica*, vol. 32, no. 3, pp. 442–455, 2016.

[29] Z. Zhang, R. Zhang, H. Xie, J. Liu, and P. Were, "Differences in the acoustic emission characteristics of rock salt compared with granite and marble during the damage evolution process," *Environmental Earth Sciences*, vol. 73, no. 11, pp. 6987–6999, 2015.

[30] C. Zhao, C. Bao, H. Matsuda, C. F. Zhao, and J. S. Tian, "Application of digital image correlation method in experimental research on crack propagation of brittle rock," *Chinese Journal of Geotechnical Engineering*, vol. 37, no. 5, pp. 944–951, 2015.

[31] H. Munoz, A. Taheri, and E. K. Chanda, "Pre-peak and post-peak rock strain characteristics during uniaxial compression

by 3D digital image correlation," *Rock Mechanics and Rock Engineering*, vol. 49, no. 7, pp. 2541–2554, 2016.

[32] J.-L. Cheng, S.-Q. Yang, K. Chen, D. Ma, F.-Y. Li, and L.-M. Wang, "Uniaxial experimental study of the acoustic emission and deformation behavior of composite rock based on 3D digital image correlation (DIC)," *Acta Mechanica Sinica*, vol. 33, no. 6, pp. 999–1021, 2017.

[33] S.-Q. Yang, Y.-H. Huang, W.-L. Tian, P.-F. Yin, and H.-W. Jing, "Effect of high temperature on deformation failure behavior of granite specimen containing a single fissure under uniaxial compression," *Rock Mechanics and Rock Engineering*, vol. 52, no. 7, pp. 2087–2107, 2019.

[34] A. V. Mikhalyuk and V. V. Zakharov, "Dissipation of dynamic-loading energy in quasi-elastic deformation processes in rocks," *Journal of Applied Mechanics and Technical Physics*, vol. 38, no. 2, pp. 312–318, 1997.

[35] Q. Guo, J. Pan, M. Cai, and Y. Zhang, "Analysis of progressive failure mechanism of rock slope with locked section based on energy theory," *Energies*, vol. 13, no. 5, p. 1128, 2020.

[36] H. Xie, L. Li, R. Peng, and Y. Ju, "Energy analysis and criteria for structural failure of rocks," *Journal of Rock Mechanics and Geotechnical Engineering*, vol. 1, no. 1, pp. 11–20, 2009.

[37] H. Xie, L. Li, Y. Ju, R. Peng, and Y. Yang, "Energy analysis for damage and catastrophic failure of rocks," *Science China Technological Sciences*, vol. 54, no. 1, pp. 199–209, 2011.

[38] M. Cai, "Prediction and prevention of rockburst in metal mines—a case study of Sanshandao gold mine," *Journal of Rock Mechanics and Geotechnical Engineering*, vol. 8, no. 2, pp. 204–211, 2016.

[39] F.-q. Gong, S. Luo, and J.-y. Yan, "Energy storage and dissipation evolution process and characteristics of marble in three tension-type failure tests," *Rock Mechanics and Rock Engineering*, vol. 51, no. 11, pp. 3613–3624, 2018.

[40] F. Gong, J. Yan, S. Luo, and X. Li, "Investigation on the linear energy storage and dissipation laws of rock materials under uniaxial compression," *Rock Mechanics and Rock Engineering*, vol. 52, no. 11, pp. 4237–4255, 2019.

[41] S.-q. Yang, H.-m. Ni, and S. Wen, "Spatial acoustic emission evolution of red sandstone during multi-stage triaxial deformation," *Journal of Central South University*, vol. 21, no. 8, pp. 3316–3326, 2014.

[42] Q. Meng, M. Zhang, L. Han, H. Pu, and T. Nie, "Effects of acoustic emission and energy evolution of rock specimens under the uniaxial cyclic loading and unloading compression," *Rock Mechanics and Rock Engineering*, vol. 49, no. 10, pp. 3873–3886, 2016.

[43] Q. Meng, M. Zhang, L. Han, H. Pu, and Y. Chen, "Acoustic emission characteristics of red sandstone specimens under uniaxial cyclic loading and unloading compression," *Rock Mechanics and Rock Engineering*, vol. 51, no. 4, pp. 969–988, 2018.